URANOS — Low-Energy Photon Beamline for ARPES Measurements

N. Olszowska[a,*], D. Wutke[a,b], M. Rosmus[c], R. Kurleto[a] and J.J. Kołodziej[b]

[a]*National Synchrotron Radiation Centre (NRSC) SOLARIS, Jagiellonian University, Czerwone Maki 98, 30-392 Kraków, Poland*
[b]*Faculty of Physics, Astronomy and Applied Computer Science, Jagiellonian University, S. Łojasiewicza 11, 30-348 Kraków, Poland*
[c]*Université Paris-Saclay, CNRS, Institut des Sciences Moléculaires d'Orsay, Orsay 91405, France*

Received: 18.12.2025 & Accepted: 12.06.2026

Doi: 10.12693/APhysPolA.149.S235 *e-mail: natalia.olszowska@uj.edu.pl

The Ultra-Resolved ANgular phOtoelectron Spectroscopy (URANOS) beamline is a dedicated facility for spin- and angle-resolved photoemission spectroscopy at the SOLARIS synchrotron. Over a photon energy range of 8–150 eV, the beamline provides high photon flux, tunable polarization, and few-meV energy resolution. The higher harmonic contamination stays below 1%. Photon beams of lower quality may be generated up to 600 eV energy. The photon beam is focused to approximately 150 μm (horizontally) $\times$ 60 μm (vertically) and may be further cut down to 60 μm $\times$ 60 μm at the sample. The available instrumentation enables angle-resolved photoemission spectroscopy measurements at temperatures ranging from 500 down to 4 K.

topics: angle-resolved photoemission spectroscopy (ARPES) beamline, SOLARIS synchrotron

1. Introduction

The Ultra-Resolved ANgular phOtoelectron Spectroscopy (URANOS) beamline at the SOLARIS Centre is designed for high-resolution electronic structure studies of solids and their surfaces using angle-resolved photoemission spectroscopy (ARPES) and spin- and angle-resolved photoemission spectroscopy (spin-ARPES). Covering a photon energy range of 8–150 eV with full polarization control, the beamline combines high photon flux, high energy and angular resolution, and harmonic suppression. Since its commissioning in 2018, URANOS has undergone significant automation and instrumentation upgrades to support advanced photoemission experiments. This article summarizes the current configuration, performance parameters, and capabilities of the beamline. A separate publication will detail the recently installed spin-filter detection system and will describe the end station in more detail.

ARPES is one of the most powerful experimental techniques for investigating the electronic structure of condensed matter systems. In an ARPES experiment, the kinetic energy (E_{kin}) and emission angles of photoemitted electrons are measured. Within the sudden approximation, these experimentally accessible quantities can be directly related to the binding energy (E) and crystal momentum ($\hbar\boldsymbol{k}$) of the electronic initial states in the solid. When sufficient photoelectron statistics are measured, ARPES enables the reconstruction of the electronic band dispersion $E(\boldsymbol{k})$, providing direct access to the occupied band structure of materials.

When combined with spin-selective detection, spin-resolved ARPES (spin-ARPES) additionally provides information about the electron spin polarization (σ). As a result, the complete set of quantum numbers characterizing the electronic states — energy, momentum, and spin (respectively, E, $\boldsymbol{k}$, and σ) — can be experimentally determined. Such multidimensional access to the electronic structure is essential for studying modern quantum materials, including topological insulators, Rashba systems, strongly correlated materials, low-dimensional systems, and unconventional superconductors.

The URANOS beamline has been designed to enable efficient and high-resolution mapping of electronic states in the full $(E, \boldsymbol{k}, \sigma)$ parameter space. The combination of tunable photon energy, variable light polarization, high photon flux, and spin-resolved detection capabilities provides a versatile experimental platform for investigating complex many-body phenomena and spin-dependent electronic properties of condensed matter systems.

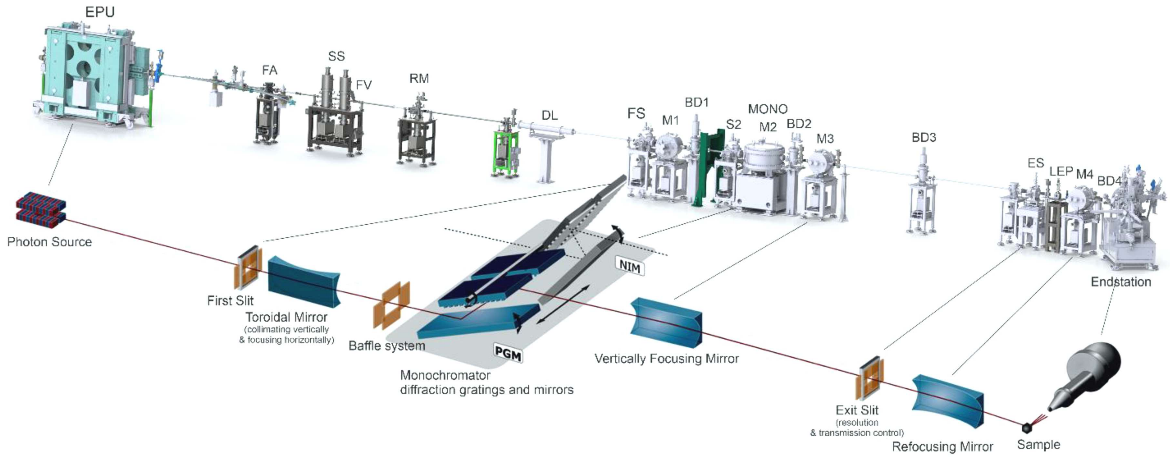

Fig. 1. Computer-aided design (CAD) model and optical layout of the URANOS beamline. The individual components are labeled as follows: EPU — elliptical polarizing undulator (Kyma), FA — fixed aperture, SS — shutter/stopper, RM — rectangular mask, DL — delay line, FV — fast-closing safety valve, FS — first slit, M1 — toroidal mirror, BD1 — beam diagnostic unit with yttrium aluminum garnet (YAG) screen, S2 — secondary slits, M2 — monochromator switching mirrors directing the beam either to the plane-grating monochromator (PGM) or the normal-incidence monochromator (NIM), BD2 — beam diagnostic unit with YAG screen and photodiode, M3 — focusing mirror, BD3 — beam diagnostic unit with YAG screen, ES — exit slit, LEP — movable mirror for the low-energy photon branch, M4 — refocusing mirror, and BD4 — beam diagnostic unit with YAG screen and photodiode.

In addition to ARPES and spin-ARPES, URANOS offers a few other experimental techniques, namely: circular dichroic ARPES (CD-ARPES), X-ray photoelectron spectroscopy (XPS) up to 500 eV, grazing-incidence and total-reflection XPS (GI/TR-XPS), and low-energy electron diffraction (LEED) for surface crystallography.

2. Facility overview and beamline concept

2.1. SOLARIS storage ring

SOLARIS is a third-generation synchrotron radiation facility based on a low-energy, high-brightness electron storage ring constructed as a replica of the MAX IV 1.5 GeV storage ring. The nominal electron-beam energy is 1.5 GeV [1, 2]. The storage ring is optimized for the generation of high-brilliance synchrotron radiation, with beam brightness being strongly dependent on the transverse electron-beam emittance.

The natural horizontal emittance of the SOLARIS storage ring is 5.98 nm rad, while the vertical emittance is more than two orders of magnitude smaller [1, 3]. Such low emittance values enable the production of highly collimated and high-brightness photon beams required for advanced experiments.

The storage ring has a circumference of 96 m and consists of twelve double-bend achromat (DBA) lattice cells incorporating fully integrated combined-function magnets. This lattice design allows for a compact ring construction while maintaining low electron-beam emittance and excellent beam stability [4, 5]. The ring includes ten straight sections dedicated to insertion devices, enabling the operation of multiple synchrotron beamlines with diverse experimental capabilities.

2.2. General beamline layout

The beamline receives radiation from an APPLE-II-type elliptically polarizing undulator installed in one of the SOLARIS storage ring straight sections. The emitted synchrotron radiation is transported through the front-end and collimating optics toward monochromators, which provide monochromatic radiation with tunable photon energy. Refocusing optics located downstream of the monochromator deliver the photon beam onto the sample in the experimental endstation. The beamline layout and its components are shown in Fig. 1.

3. Photon source

3.1. Quasiperiodic APPLE-II EPU

The photon source of the URANOS beamline is a quasiperiodic APPLE-II-type elliptically polarizing undulator (EPU). The magnetic structure consists of four Halbach arrays composed of NdFeB permanent magnet blocks mounted on four independent sub-girders. Each undulator period comprises four magnet blocks per array. The upper and lower

TABLE I

Key EPU parameters.

Parameter	Value
Undulator type	APPLE II, quasiperiodic
Operating modes	parallel and antiparallel
Available polarizations	linear (horizontal, vertical, or skewed); circular (left and right); elliptical
Undulator period length λ_0	120 mm
Number of periods	21
Undulator length L_u	2660 mm
Magnet material	NdFeB (remanence $B_r > 1.26$ T and coercivity $H_cB > 11.9$ kOe)
Saturation field B_s of NdFeB magnets	1.24 T
Magnetic field $B_{\max}$ at 18 mm gap	0.774 T (vertical); 0.501 T (circular); 0.649 T (horizontal)
Minimum–maximum gap on axis	18–220 mm (software limit 20–200 mm)
Minimum photon energy (1st harmonic)[†2]	$\sim$ 7.6 eV (gap 20 mm, horizontal phase); $\sim$ 4.3 eV (gap 18 mm)
Undulator parameter $K = \frac{eB_0\lambda_0}{2\pi m_e c} \approx 0.934\, B_0\,[\mathrm{T}]\ \ \lambda_0\,[\mathrm{cm}]$	e.g., $K \approx 6.72$ (at 0.6 T), $K \approx 8.96$ (at 0.8 T)
Phase shift range	± 60 mm corresponds to $\frac{1}{2}\lambda_0$
Gap and phase shift reproducibility	0.5 μm

sub-girders belonging to one diagonal pair can be longitudinally shifted with respect to the remaining arrays.

By varying the relative phase shift between the magnet arrays[†1], the orientation and ellipticity of the generated magnetic field can be continuously controlled. This enables flexible tuning of the photon polarization to the linear and circular polarization modes (see also Sect. 9 in this paper and the example of a variable-polarized excitation photoemission experiment shown there).

The undulator operates in a quasiperiodic configuration of magnets to suppress higher-order harmonics in the emitted photon spectrum. This is particularly important for the unambiguous interpretation of photoemission spectra and better visibility of the less intense spectral features.

The main parameters of the undulator are summarized in Table I[†2].

[†1]The EPU may operate both in parallel and in antiparallel modes. In the parallel mode, the upper and lower diagonal magnet arrays are shifted in the same direction, enabling the generation of horizontal, vertical, circular, and elliptical polarization. In the antiparallel mode, the upper and lower magnet arrays are shifted in opposite directions, resulting in linearly polarized light at oblique angles (skew polarization) [6].

3.2. Gap–energy calibration

Figure 2 shows the experimentally determined dependence of the fundamental (first-harmonic) photon energy on the undulator gap for several phase-shift configurations, resulting in linear horizontal, linear vertical, circular, and two elliptical polarizations of light. The calibration curves were fitted using fifth-order polynomial functions, whose coefficients are implemented in the beamline control system for automatic calculation of the undulator settings corresponding to the requested photon energy and polarization state.

[†2]Photon energy in the first harmonic (defined by the radiation wavelength of the emitted photon, λ_r) is given by $E_1 = \dfrac{hc}{\lambda_r} = \dfrac{hc}{\frac{\lambda_0}{2n\gamma^2}\left(1+\frac{K^2}{2}+\gamma^2\theta^2\right)}$, where n is the harmonic number, γ is the Lorentz factor of the electron beam, K is the undulator deflection (strength) parameter, and θ is the observation angle relative to the undulator axis. For the center of the emission cone ($\theta = 0$), $E_1 = \dfrac{2hc\gamma^2}{\lambda_0\left(1+\frac{K^2}{2}\right)}$. The Lorentz factor for an electron beam energy in NSRC SOLARIS ($E_e = 1.5$ GeV) is $\gamma = E_e/(m_e c^2) \approx 2936$.

4. Beamline optics and photon transport

4.1. Front-end and safety system

The front-end (FE) connects the beamline to the storage ring and defines the initial angular acceptance of the photon beam first with a fixed circular aperture (FA) of 2 mrad, and then with a movable rectangular mask (RM) with an opening of 1×1 mrad^2. A fast-closing safety valve (FV), triggered by the vacuum interlock system in case of accidental air inrush, protects the storage ring vacuum and closes within milliseconds. A dedicated delay-line chamber (DL) is installed upstream of the valve to reduce the propagation speed of pressure shock waves. Two interlocked shutter–stopper (SS) assemblies are used to block all radiation, including high-energy bremsstrahlung, when the beamline is inactive or during an emergency.

4.2. Optical layout

The optical system of the URANOS beamline is designed to deliver a highly monochromatic and tightly focused photon beam to the sample using a combination of mirrors, diffraction gratings, apertures, and precision slits. The beamline layout (see Fig. 1) consists of the following main optical elements (unless stated otherwise, positions are given relative to the undulator center):

(i) First slit (FS) [15.37 m] — defines the beam acceptance typically to 0.5×0.5 mrad^2.

(ii) Toroidal mirror (M1) [16.0 m] — vertically collimates the beam and horizontally focuses it onto the exit slit plane.

(iii) Baffle system (S2) [17.72 m] — provides additional limitation of the angular beam acceptance when required.

(iv) Combined monochromator stage (MONO) [18.7 m] (see Fig. 2) — consists of a plane-grating monochromator (PGM) and a normal-incidence monochromator (NIM) parts, implemented as two interchangeable mirror (M2)–diffraction grating pairs.

(v) Focusing mirror (M3) [20.0 m] — vertically focuses the beam onto the exit slit and compensates for small misalignments between the grating and mirror M2. For each photon energy and c_{ff} setting, the pitch angle of M3 is automatically adjusted to maintain the beam on the optical axis.

(vi) Micrometric exit slit system (ES) [26.0 m] — defines the photon beam energy resolution. The horizontal slit blades additionally serve as wing photocurrent collectors for beam-position monitoring and automatic correction.

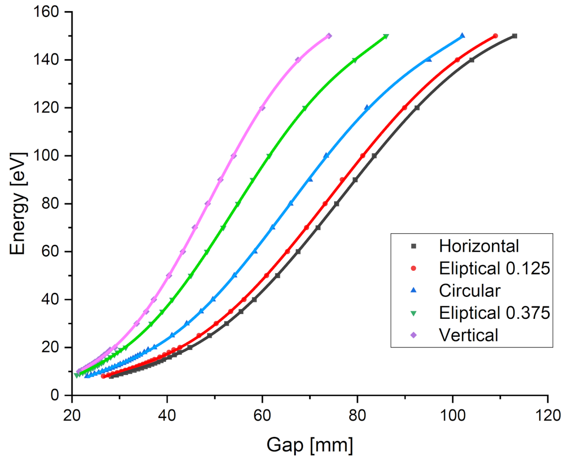

Fig. 2. The photon energy dependence on the undulator gap and phase for the first harmonic at the URANOS beamline. For antiparallel undulator modes corresponding to skew polarization, the photon energy–gap dependence was not calibrated experimentally due to the practically unlimited number of possible phase-shift configurations.

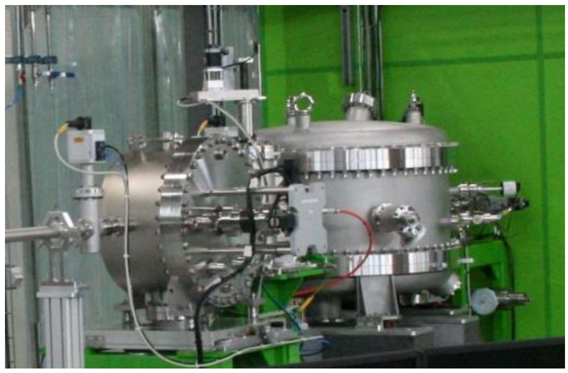

Fig. 3. Monochromator chamber (containing PGM and NIM optical elements) at the URANOS beamline. In front, the M3 mirror chamber is seen.

(vii) Movable mirror for the low-energy photon (LEP) branch — is a flat Au-coated silicon mirror mounted on a linear translator at 45° to the photon beam axis, enabling extraction of low-energy UV/VUV radiation for applications beyond photoemission spectroscopy. The mirror deflects the beam toward an MgF_2 window and a DN40CF port, allowing connection to external experimental equipment.

(viii) Refocusing mirror (M4) [27.25 m] — provides one-to-one imaging of the exit slit onto the sample position.

All mirrors, except M2, operate in vertical orientation (i.e., deflecting the beam in the horizontal plane) and are mounted on high-precision motorized stages equipped with encoders, enabling accurate control of pitch, roll, and yaw angles. In addition,

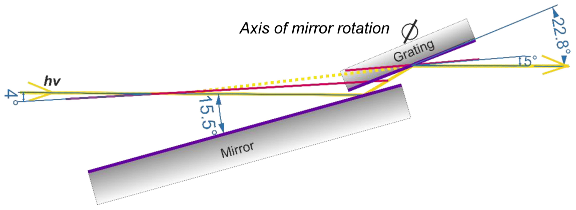

Fig. 4. Geometry of the PGM monochromator showing two allowed angular configurations of the grating and mirror. Two limiting configurations are shown in raspberry and purple colors. The beam central ray is denoted with a yellow line. The grid rotation axis is located on the grid surface, while the mirror rotation axis is positioned away from the mirror surface and is indicated by a crossed-out circle.

each mirror assembly includes manual translation stages for alignment purposes. The mirrors are fabricated from silicon substrates coated with 30 nm of gold in order to maximize reflectivity in the vacuum ultraviolet (VUV) and soft X-ray photon energy range.

The majority of the undulator radiative power is absorbed by the entrance aperture system (FA, RM, FS) and mirror M1. Mirror M1 receives ≈ 65 W of incident radiation and absorbs about 15 W. To ensure efficient heat dissipation, the FA, RM, FS, M1, and MONO are water-cooled, and the heat-loaded optical elements are properly contacted with their cooled mounts using indium interfaces. Due to its near-normal incidence geometry, the NIM mirror absorbs up to ≈ 50 W of power, whereas the PGM mirror typically absorbs between 10 and 30 W, depending on operating conditions. All critical optical components are mounted on vibration-damped support structures to ensure long-term mechanical stability and reproducible beam alignment.

4.3. Beam diagnostics stations

Beam diagnostics (BD) stations are distributed along the beamline to enable continuous monitoring of beam position, shape, intensity, and optical alignment. Key systems include:

(i) FS — by measuring the photocurrent from four electrically isolated plates, the device operates as a beam-position monitor (BPM).

(ii) BD1 (downstream of M1) — equipped with a YAG fluorescent screen used for M1 alignment and monitoring of the undulator radiation profile. Since BD1 may be exposed to heat loads approaching 50 W, operation requires careful thermal management. Note that BD1, the front-end diagnostics system (FEDS), and M1 are located inside the radiation safety hutch.

(iii) Baffle system (S2) — by reading the photocurrent from four electrically isolated plates, it operates as a beam-position monitor (BPM).

(iv) BD2 (downstream of the monochromator) — equipped with a YAG screen and photodiode AXUV576C for inspection of the monochromatized beam profile and photocurrent measurements.

(v) BD3 (downstream of M3) — includes a YAG screen enabling further inspection of the beam.

(vi) Exit slit and PID control of the beam — the horizontal slit blades measure wing photocurrents and may be used to define the horizontal beam size. The wing photocurrent signals are used within a proportional–integral–derivative (PID) feedback loop to stabilize the beam position horizontally during photon-energy scans and to compensate for long-term beam drifts (through automatic M3 pitch correction).

(vii) BD4 (downstream of M4) — equipped with a YAG screen and an XUV-035 photodiode used for characterization of the monochromatic photon beam incident on the sample position.

5. Dual monochromator system

5.1. Dual-monochromator concept

The beamline features a dual monochromator system:

(i) PGM operating on a collimated beam, designed for the 16–100 eV photon energy range, comprising a 600 l/mm grating.

(ii) NIM working within the photon energy range 8–30 eV, providing a beam of high spectral purity (harmonic suppression) and conserving the beam polarization, comprising a 2000 l/mm grating.

Both monochromators use single laminar plane gratings, fabricated from silicon substrates and coated with ≥ 30 nm of gold. The monochromators operate in the vertical dispersion plane. Switching between PGM and NIM configurations is achieved by translating the entire monochromator chamber horizontally, and transversally to the light beam (see Fig. 3). This dual-geometry approach allows for flexible optimization of photon beam properties, including energy range, spectral resolution, harmonic suppression, photon flux, and polarization. The monochromator system does not need an optical entrance slit since the undulator source is confined spatially rather well by itself.

Across their design energy ranges, both monochromators achieve resolving powers (RP) up to 20000, corresponding to a photon energy resolution of ~ 1 meV at the lowest photon energies.

5.2. Plane grating monochromator (PGM)

PGM operating at grazing incidence (see Fig. 4) provides high photon flux. It is particularly efficient at photon energies > 20 eV. In practical use, the device allows for a wider-than-designed photon energy range, i.e., 11.5–600 eV; however, the design specifications (5×10^{11} photons/s at the resolving power of 20000) are not necessarily met outside the design range, i.e., 16–100 eV.

The conceptual scheme of PGM is shown in Fig. 4. The optical elements are rotated in such a way that the beam always exits parallel to the incoming beam, with a constant offset and a constant focal point. This greatly simplifies subsequent beam handling within the beamline's optical system.

5.3. Normal-incidence monochromator (NIM)

In NIM geometry (see Fig. 5), the included angle is fixed at $\varphi = \alpha - \beta = 14°$, determined by the static mirror configuration.

5.4. Energy range, polarization fidelity, and harmonic suppression

For a diffraction grating, the photon wavelength and energy are governed by the grating equation

$$\lambda = \frac{hc}{E} = \frac{\sin(\alpha) + \sin(\beta)}{N\,k}, \tag{1}$$

where α and β are, respectively, the incidence and diffraction angles measured with respect to the grating normal (assigned the opposite signs if measured on the opposite sides of the normal), N is the groove density[†3], and k denotes the diffraction order.

The principal operational parameter of the PGM is the fixed-focus constant $c_{ff} = \cos(\beta)/\cos(\alpha)$. Owing to the collimated-beam design, the c_{ff} parameter can be changed without changing the exit slit position.

The influence of c_{ff} on energy resolution is moderate. In routine operation, a value of $c_{ff} = 1.8$ is typically used over a broad range of the photon energies 17–70 eV. At lower photon energies (< 17 eV), higher c_{ff} values are required due to mechanical constraints associated with grating and mirror motions. At higher photon energies ($h\nu > 70$ eV), lower c_{ff} values, typically around 1.2, maximize monochromator transmission at the expense of spectral resolution. In practice, this reduction in resolution can be compensated by decreasing the exit slit width.

[†3]Here, 600 lines/mm for PGM and 2000 lines/mm for NIM.

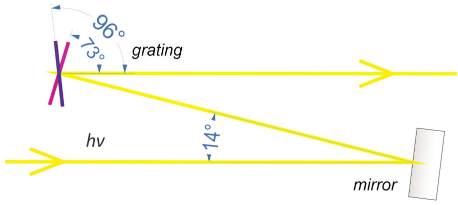

Fig. 5. Geometry of the NIM monochromator showing two limiting angular configurations of the grating. The mirror plane is oriented at an angle of 83° to the incident beam.

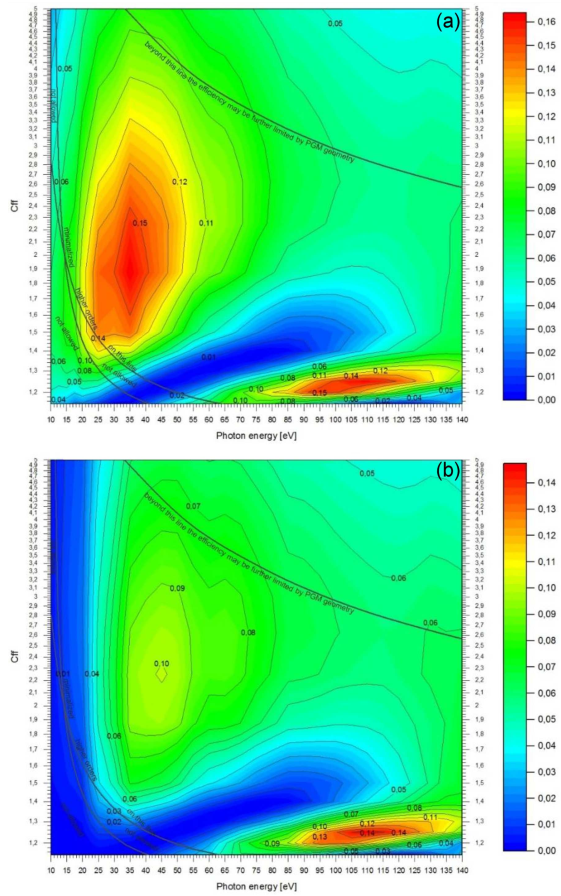

Fig. 6. Calculated efficiency (transmittance) maps of the URANOS PGM for horizontally polarized light (a) and vertically polarized light (b). The superimposed lines indicate the mechanical operating limits of the monochromator. The transmittance includes both the first-order diffraction efficiency of the grating, calculated using the open-source software developed by Mark Boots [7], and the reflectivity of the plane mirror [8]. The rigorous electromagnetic calculation is possible only for the horizontally polarized light using the open software. For vertically polarized light, the transmittance was estimated by scaling the horizontally polarized results using appropriate polarization-dependent reflectivity ratios. Benchmark comparisons with available reference data indicate that this approximation introduces deviations smaller than ≈ 10%.

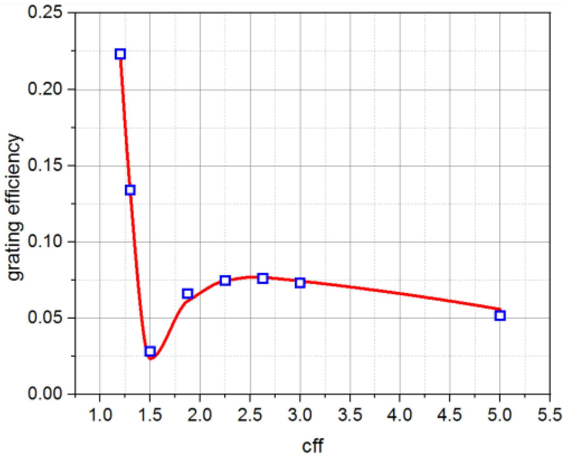

Fig. 7. Comparison between theoretical and experimental efficiency functions of the URANOS PGM. The red curve was extracted from the calculated efficiency map shown in Fig. 5a for a constant photon energy of 100 eV. The blue experimental data points correspond to photoelectron signal intensities measured at constant energy resolution and normalized to the reflectance of all contributing mirrors. The amplitude of the experimental curve was scaled to facilitate direct comparison, demonstrating also a very good agreement between the calculated and measured monochromator efficiency functions.

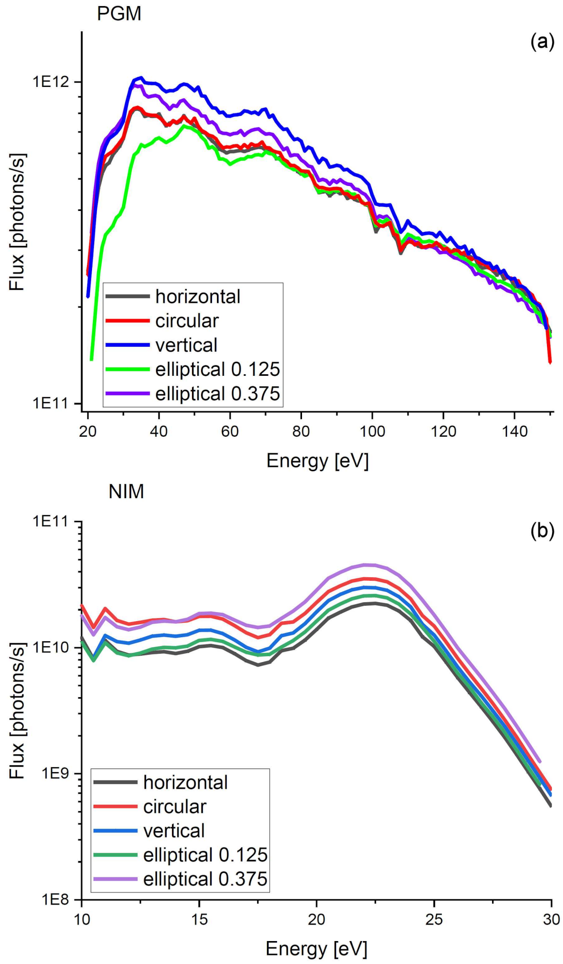

Fig. 8. Photon flux measured at the BD4, located upstream of the endstation, using an XUV-035 photodiode for different photon polarization modes. The measurements were performed with vertical slit openings of 25 μm (250 μm) and horizontal slit openings of 300 μm (500 μm) for the PGM (NIM) monochromators, respectively, as shown in panel (a) (panel (b)), at a stored ring current of 400 mA. The measured photon flux was normalized to a resolving power of RP $= E/\Delta E = 20000$.

Figure 6 shows the efficiency maps of the PGM for horizontal and vertical polarization, depending on the combination of radiation energy $h\nu$ and c_{ff} (see also [7] and [8]). The map in Fig. 6a, for the horizontally polarized light, was obtained using rigorous electromagnetic calculations based on the measured geometry of the delivered PGM grating. The calculated transmission characteristics were experimentally verified by comparison with measured beamline transmittance data (Fig. 7) and found to reproduce the actual performance of the URANOS PGM with high accuracy.

The map shown in Fig. 6b, corresponding to vertically polarized radiation, was obtained using approximate methods (see caption for details). Nevertheless, it reproduces the principal transmission characteristics with sufficient accuracy for practical analysis.

As seen in Fig. 6b, vertically polarized radiation cannot be transmitted efficiently below 25 eV for any setting of c_{ff}. Consequently, circularly polarized radiation transmitted through the PGM in this energy range emerges predominantly horizontally polarized. This limitation is largely absent in the NIM geometry, where horizontal and vertical polarization components are transmitted with comparable efficiency.

Despite careful optimization of the c_{ff} parameter, harmonic contamination in the grazing-incidence PGM geometry remains significant at low photon energies, leading to elevated photoemission background signals. In this regime, the NIM monochromator becomes preferable due to its intrinsically superior higher-order suppression and improved spectral purity.

Owing to the normal-incidence geometry, the practical operating range of NIM is limited to ≈ 8–22 eV as a consequence of reduced mirror reflectivity and overall optical throughput at higher photon energies. Although NIM provides a considerably lower photon flux compared to PGM (see Fig. 8), it is often advantageous for experiments below 20 eV, where efficient harmonic suppression is essential to avoid spectral artifacts originating from deep electronic states excited by higher-order radiation.

In addition, NIM preserves the polarization state of the incoming radiation significantly better than PGM.

6. Beamline performance

6.1. Photon flux

The measured photon flux at the sample position for different photon energies and polarization modes of the undulator first harmonic is presented in Fig. 8. The total photon flux measured in front of the endstation reflects the source intensity modified by the cumulative transmission of the entire optical system, including mirror reflectivities, grating diffraction efficiency, and exit slit transmission. The measured flux values confirm that the monochromator design goals were successfully achieved[†4].

6.2. Energy resolution model

The contribution of the exit slit opening to the overall beamline energy resolution can be expressed as

$$\Delta E_{\text{exit slit}} = \Delta S_{\text{exit slit}} \, \frac{E^2 \cos(\beta)}{1239.84 \, N \, q \, k}, \tag{2}$$

where $\Delta S_{\text{exit slit}}$ denotes the exit slit width, $q = 6$ m is the distance between the focusing mirror and the exit slit. The diffraction angle β is related to the incidence angle α via the fixed-focus constant c_{ff} as follows $\cos(\beta) = c_{ff} \cos(\alpha)$.

Another contribution to the resolution is the diffraction (resolving-power) limit. The diffraction-limited Rayleigh wavelength resolution for a grating can be expressed as

$$\Delta\lambda_{\min} \approx \frac{\lambda}{k \, N \, l}, \tag{3}$$

which in energy units becomes

$$\Delta E_{\text{diff}} = \frac{E}{k \, l \, N}, \tag{4}$$

where l is the illuminated length of the grating. For a beam with the full width at half maximum (FWHM), d, at the grating, the illuminated length can be approximated as $l = d/\cos(\alpha)$, so the diffraction limit improves with increasing illuminated length and higher groove density.

Another contribution to resolution arises from the finite source size. The beamline focusing optics produces an image of the source at the exit slit; this image width contributes to the transmitted photon-energy bandwidth in the same manner as a finite slit width. If Δ_{src} denotes the vertical source size (FWHM, in mm) and M the image magnification (such that the image size at the slit plane is $M\Delta_{src}$), then the source-size contribution to the energy resolution can be expressed as follows

$$\Delta E_{\text{source}} = (M \Delta_{src}) \, \frac{E^2 \cos(\beta)}{1239.84 \, N \, q \, k}. \tag{5}$$

Since the diffraction plane is vertical, only the vertical-plane-projected beam properties are relevant for the URANOS beam monochromatization. The beamline optics provides a vertical geometrical magnification given by $M = \frac{q}{p} \, c_{ff}$, where p is the distance from the source to the collimating M1 mirror (16 m), and q is the distance between the focusing mirror M3 and the exit slit (6 m). The beam is vertically collimated between M1 and M3 mirrors, so this part is irrelevant for the magnification discussed here.

The source size Δ_{src} can be approximated as a convolution (i.e., the quadratic sum of spatial uncertainties) of the electron beam size in the undulator and the diffraction-limited size of the undulator radiation field.

Only the vertical electron-beam emittance (i.e., the product of beam size and divergence) is relevant for the URANOS beam monochromatization. However, both the spatial and angular electron-beam contributions are negligible compared to the corresponding angular and spatial characteristics of the undulator photon source (in vertical projection). Consequently, the URANOS synchrotron radiation is diffraction-limited in the vertical plane. As a result, the monochromatic beam properties (e.g., transmission, photon energy bandwidth, and resolution) are essentially insensitive to imperfections of the electron beam.

Every optical element introduces manufacturing imperfections and may exhibit mechanical or thermal deformations (slope errors), leading to

TABLE II

RMS slope errors of the beamline optical elements.

Optical element	RMS slope error	Plane
M1 collimating mirror	2.59 μrad	sagittal[†5]
M2 plane mirror	0.534 μrad	tangential
GR grating	0.9 μrad	tangential
M3 focusing mirror	3.59 μrad	sagittal[†5]

[†4]For the PGM, the grating efficiency for horizontally polarized radiation exceeds 20% at photon energies around 35 eV. In the case of the NIM, the grating efficiency reaches ≈ 3–5% within the operational photon energy range 8–20 eV. The transmittance ratio of NIM vs PGM is further reduced several times, with a low reflection efficiency of the NIM plane mirror (∼ 20%).

[†5]For vertically oriented mirrors (with the sagittal relevant plane), their slope errors enter the resolution formulas multiplied by sin(2°) (beam incidence angle) to account for their specific geometry.

TABLE III

Calculated examples of theoretical resolution on the URANOS beamline.

Parameters	Unit	PGM								NIM	
Photon energy	eV	12	12	20	20	50	50	100	100	8	8
Exit slit	μ m	50	500	50	200	50	200	50	50	100	500
c_{ff}		2.5	2.5	1.8	1.8	1.8	1.8	1.2	2.5	–	–
Slit contribution	meV	0.6	6.1	1.4	5.8	5.8	23.1	24.5	14.9	0.4	2
Slope error	meV	0.2	0.2	0.6	0.6	2.3	2.3	11.7	5.1	0.1	0.1
Diffraction limit	meV	0.4	0.4	1	1	2.6	2.6	11.5	3.4	0.2	0.2
Source contribution	meV	0.4	0.4	1.1	1.1	2.9	2.9	13	3.8	0.3	0.3
Total error	meV	0.9	6.1	2.2	6	7.3	23.5	32.2	16.5	0.54	2.06

deviations in the reflection angle. These effects must also be accounted for. There are four optical elements in the optical path (see Table II, where the relevant root-mean-square (RMS) slope errors are given).

Using formulas from the work of Follath et al. [9], the resolving power R can be defined for each optical element in the system.

For the grating, one obtans

$$R_{gr} = \frac{\sin(\alpha) + \sin(\beta)}{\left|\cos(\beta) - \cos(\alpha)\right| \sigma_{gr}}. \qquad (6)$$

For M1 (collimating) and M3 (focusing), Follath et al. [9] introduced the so-called angle transfer coefficient $T(c_{ff})$, which quantitatively relates the local slope error of an optical element to the effective variation of the incidence or diffraction angle on the grating as[†6]

$$T(c_{ff}) = \sqrt{\frac{\lambda\, k\, N \left(c_{ff}^2 - 1\right)}{2}}. \qquad (7)$$

If M1 causes an effective change in the angle of incidence $\delta\alpha = T_{\mathrm{M1,M2}}\, \delta\theta_{\mathrm{M1,M2}}$, then the contribution to the relative energy variation is (analogously to the expression (7))

$$\frac{\Delta E_{\mathrm{M1}}}{E} = \frac{\cos(\alpha)}{\sin(\alpha) + \sin(\beta)}\, T_{\mathrm{M1}}\, \sigma_{\mathrm{M1}}. \qquad (8)$$

An analogous equation can be written for M3. This yields the following resolving powers for the individual optical elements, namely

$$R_{gr} = \frac{1}{\sigma_{gr}(1 + c_{ff})}\, T(c_{ff}), \qquad (9)$$

$$R_{\mathrm{M1,M2}} = \frac{1}{\sigma_{\mathrm{M1,M2}}}\, T(c_{ff}), \qquad (10)$$

$$R_{\mathrm{M3}} = \frac{1}{\sigma_{\mathrm{M3}}} \frac{1}{c_{ff}}\, T(c_{ff}). \qquad (11)$$

The total contribution from slope errors (RSS) can be written as

$$\Delta E_{\mathrm{slop}} = \sqrt{\Delta E_{\mathrm{M1}}^2 + \Delta E_{gr}^2 + \Delta E_{\mathrm{M2}}^2 + \Delta E_{\mathrm{M3}}^2} =$$

$$\frac{10^{-6} \times E}{T(c_{ff})} \sqrt{1.33 + 1.62\, c_{ff} + 0.83\, c_{ff}^2}. \qquad (12)$$

The total energy resolution is the sum of all contributions,

$$\Delta E_{tot} = \sqrt{\Delta E_{\mathrm{source}}^2 + \Delta E_{\mathrm{slit}}^2 + \Delta E_{\mathrm{slope}}^2 + \Delta E_{\mathrm{diffraction}}^2}. \qquad (13)$$

Example calculations for different values of c_{ff} and photon energy are presented in Table III. A dedicated macro for calculating the beamline resolution for user-defined experimental parameters is available at the beamline.

6.3. Experimental resolution verification

Theoretically estimated photoelectron energy resolutions are consistent with those measured at the endstation using the DA30L analyzer, which provides guaranteed minimum energy resolutions of 1.8, 3.6, and 6 meV for pass energies of 2, 5, and 10 eV, respectively, with an entrance slit width of < 300 μm.

Figure 9 shows the measured Fermi edge of polycrystalline gold at cryogenic temperatures. Such spectra are used most often to determine the experimental resolution in photoemission experiments. This method of resolution estimation is, however, relatively uncertain, particularly in the few-meV regime, because the photon bandwidth, thermal broadening of the Fermi edge, and the electron spectrometer resolution all contribute to the observed step width to a comparable extent. A clearer determination of the energy resolution, but only for NIM, for photon energies of ~ 10 eV, was obtained using the gas cell past the MgF_2 window and studying the krypton absorption line (see Fig. 10).

[†6]Using photon energy in eV instead of wavelength, one obtains: $T_{c_{ff}} = \sqrt{0.372\, \frac{({c_{ff}}^2 - 1)}{E}}$.

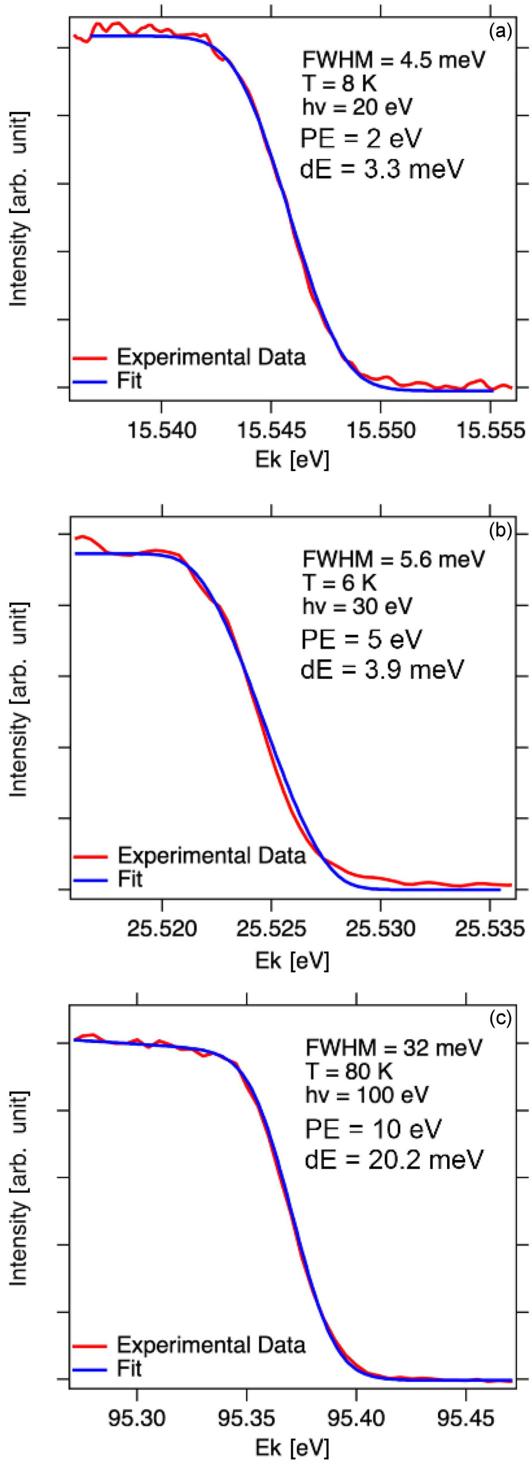

Fig. 9. Photoelectron spectrum measured at the Fermi edge of polycrystalline gold at cryogenic temperatures. The total energy resolution ($\mathrm{d}E$) is obtained by fitting the spectrum with a convolution of the Fermi–Dirac distribution and a Gaussian function. The individual spectra were obtained at different temperatures (T), photon energies ($h\nu$), and detector pass energies (PE), namely: (a) $T = 8$ K, $h\nu = 20$ eV, $PE = 2$ eV; (b) $T = 6$ K, $h\nu = 30$ eV, $PE = 5$ eV; (c) $T = 80$ K, $h\nu = 100$ eV, $PE = 10$ eV.

6.4. Beam spot at sample

The distance between the source and the sample position is 28.5 m. At the sample position, the photon beam spot size is approximately 150 μm × 60 μm (horizontally × vertically). The spot size can be further reduced to about 60 μm × 60 μm by decreasing the horizontal exit slit opening, at the cost of reduced photon flux.

In practice, the optimal configuration is selected depending on the required balance between spatial resolution, energy resolution, and count rate for a given experiment.

7. Experimental setup at the endstation

7.1. DA30-L hemispherical analyzer

The core component of the endstation is a VG Scienta DA30-L hemispherical electron spectrometer, which enables the acquisition of three-dimensional photocurrent maps $I(\theta_x, \theta_y, E)$, where θ_x and θ_y denote the emission angles in the Cartesian projection onto the xz and yz planes, respectively, in a coordinate system in which the z-axis is aligned with the main axis of the electron spectrometer (see Fig. 11). Table IV summarizes the basic parameters of the DA30-L detector.

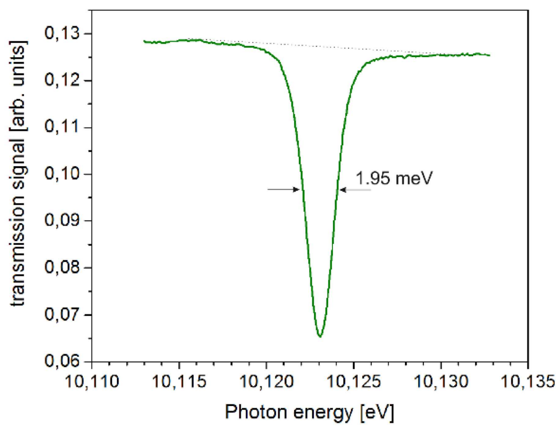

Fig. 10. Absorption spectrum of krypton around the 123 nm (10.08 eV) line recorded using NIM. Measurements were performed with an exit slit opening of 200 μm and a corresponding theoretical photon energy resolution of 1.8 meV. The data also indicate that the NIM photon energy scale is shifted by approximately 40 meV, which is not significant for the system normal function, i.e., acquiring photoelectron spectra, since they are always referred to the Fermi level. The data has been collected as a part of the HYADES project link *www.hyades.oa.uj.edu.pl*.

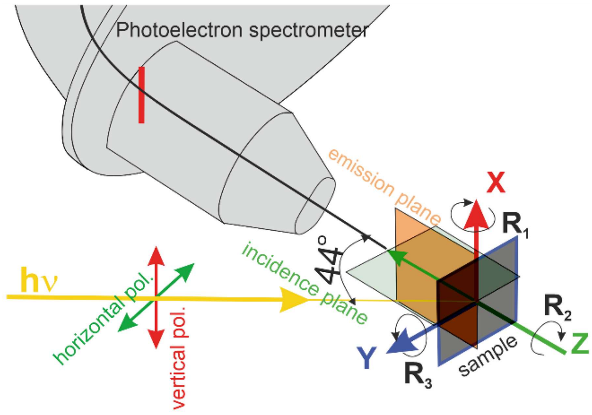

Fig. 11. Measurement geometry of the experimental setup. The angle between the spectrometer axis and the incident photon beam is 44°. The orientation of the analyzer entrance slit and the radiation polarization vectors are indicated. The excitation (incident) plane and the photoelectron emission plane are also marked.

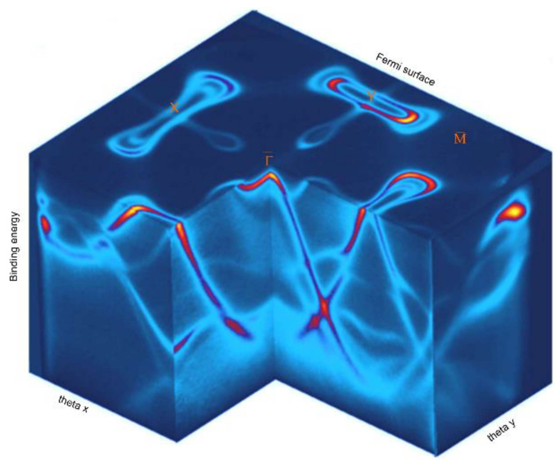

Fig. 12. The photocurrent angle-energy distribution for NbP. The NbP band structure measured in deflection mode, obtained using an excitation energy of 93.4 eV at a temperature of 78 K. The measured distribution is a 3D "map". This, obviously, can not be presented in full on the static picture. Here are shown only values on surfaces of specifically carved, rectangular block. More details can be found in [10].

The spectrometer consists of a multielement electrostatic lens entrance system, a hemispherical energy filter enabling a choice of nine entrance slits, and a two-dimensional position-sensitive electron detector. The entrance lens system is a key element of the device. It allows for switching between several measurement modes for the study of the photoelectron energy spectra either in real or angular spaces. It also incorporates two sets of electrostatic deflection plates, which are typically used to scan the accepted angle θ_y.

TABLE IV

Specifications of the VG Scienta DA30-L electron analyzer at the URANOS beamline.

Parameter	Value/Mode
Analyzer type	hemispherical DA30-L, radius 200 mm
Working distance	34 mm
Angular acceptance (full cone)	±15° (angular mode), ±19° (lens full cone)
Angular dispersive modes	±3.5°, ±7°, ±15°
Angular and momentum resolution	0.1° and 0.002–0.01 Å^{-1}
Pass energy range	2–200 eV
Guaranteed maximal energy resolution	1.8 meV at 2 eV pass energy
Entrance slit length/widths	30 mm/0.1–2.5 mm
Detector	MCP–phosphor–CCD, 40 mm diameter
Number of angular/energy channels	1000/1064

In deflection mode, the DA30-L detector can collect photoelectrons in a full 30° angular acceptance cone without mechanical sample rotation, enabling efficient mapping of photocurrent distributions in (θ_x, θ_y) angular space (see Fig. 12 and [10]). The photon incidence direction forms an angle of 44° with respect to the spectrometer axis, defining the experimental photoexcitation geometry (see Fig. 11).

7.2. Six-axis cryogenic manipulator

The spectrometer is complemented by a fully motorized six-axis cryogenic manipulator, providing three translational degrees of freedom (±12.5 mm for X/Y and ±125 mm for Z) and three rotational axes: R_1 (0°–355°, rotation around the long axis of the manipulator), R_2 (−5° to +95°, azimuthal rotation), and R_3 (−20° to +40°, polar tilt)[†7], (see Fig. 11).

Sample temperatures can be stabilized in the 4–500 K range using liquid helium or liquid nitrogen cooling combined with controlled resistive heating. The mechanical positioning accuracy and

[†7]Until 2025, the system worked with a five-axis cryogenic manipulator, including three translational axes (±12.5 mm for X/Y, ±125 mm for Z) and two rotational axes (R_1, rotation around the long axis: 0–355°; R_3, tilt polar: +2° to −126° with open radiation cover).

repeatability are ≈ 0.05 mm for translational motion and 0.1° for rotational motion, with a thermal Z-drift of ≈ 0.01 mm/°C.

The manipulator and the spectrometer are integrated within the main analytical ultra-high vacuum (UHV) chamber having a base pressure below 5×10^{-11} mbar. The system also includes an in situ sputter-cleaned gold reference pin for Fermi-level calibration.

The endstation system can store up to 24 samples under UHV conditions, ready for transfer to the main cryogenic manipulator. The system facilitates in situ sample cleaving at room temperature or at low temperatures.

7.3. Spin-resolved detection mode (VLEED Upgrad)

In 2024, a three-dimensional very-low-energy electron diffraction (VLEED)-based spin detection system was installed, extending the experimental capabilities of the endstation toward spin-resolved ARPES measurements. The upgrade is based on two VLEED spin filters, enabling simultaneous analysis of multiple spin components with substantially higher efficiency than conventional Mott detectors. A detailed technical description and performance characterization of the spin analysis system will be presented in a separate publication.

7.4. LEED and auxiliary instrumentation

The analytical chamber is additionally equipped with an MCP-based LEED system (OCI Vacuum Microengineering Inc.), supporting quantitative $I(V)$ measurements and remote data acquisition through the LIM12 MultiLEED software suite.

An ion gun is available for in-situ sputter cleaning of the gold reference pin used for Fermi-level calibration.

The system is also equipped with an acA1280-60gm Camera combined with a Computar Extender Ex2C and a 10 zoom lens system, which is highly useful for visual inspection of the sample surface, alignment procedures, and monitoring of the experimental geometry.

7.5. Sample preparation infrastructure

Samples are mounted on Omicron-type (flag-style) sample holders. Due to the tight mechanical tolerances of the transfer system and manipulators, the dimensions of the user-supplied holders should be verified and approved by the beamline staff prior to the experiment. Omicron-type holders are widely compatible with various UHV systems, including vacuum suitcases and laboratory-based preparation and analysis equipment. The system supports in-situ sample exfoliation and cleaving procedures.

The UHV preparation chamber, connected to the analytical chamber, enables a wide range of surface preparation and treatment procedures. A dedicated transfer port also allows for the connection of a vacuum suitcase for UHV sample transport between external laboratories and the beamline system.

The preparation chamber is equipped with a Mini-LEED system for preliminary surface characterization and crystallographic quality assessment.

7.5.1. Surface cleaning and annealing

Samples can be cleaned by Ar^+ ion sputtering, heated up to 1800 K, or cooled down to ≈ 100 K. Temperature control and monitoring are provided by two thermocouples (i.e., type C and type K) together with an infrared pyrometer, covering a temperature range of 250–1800°C.

7.5.2. Thin-film growth and gas dosing

The preparation chamber supports thin-film growth and gas-phase surface reactions under well-controlled thermal conditions. It is equipped with three independent retractable ports for user-supplied preparation devices, such as effusion cells or evaporators. These ports allow for rapid installation and exchange of users sources without breaking the vacuum.

Sample preparation processes can be monitored using a quartz crystal microbalance (QCM) and a residual gas analyzer (RGA). Controlled gas dosing is available through a precision leak valve and dedicated gas lines, with a maximum operating pressure during dosing of 5×10^5 mbar.

8. Control software and data workflow

8.1. Beamline and endstation control

From the early stages of the URANOS (formerly UARPES) beamline development, one of the primary goals was to achieve a high level of automation combined with an intuitive graphical user interface (GUI). As a result, the beamline is almost fully motorized and operated through a dedicated software environment.

The main applications used for beamline and experiment control include the Synoptic Panel [11], the Energy Configurator, the PID correction module, the URANOS application, and a set of smaller Tango-based tools integrated with the energy configurator and URANOS control software.

The Synoptic Panel serves as the primary operator interface for monitoring and control the beamline. It provides a graphical overview of the beamline layout and enables adjustment of key operational parameters such as photon energy, undulator phase, and exit slit opening. Basic beamline operations, including front-end and valve control, interlock reset, and beam shutter operation, are also performed directly from this interface.

The Energy Configurator and URANOS application enable:

- configuration of the monochromator photon energy ($h\nu$) and the c_{ff} parameter, including switching between PGM and NIM operation modes;
- automatic adjustment of the undulator gap and phase for the selected photon energy and polarization,
- user control of the vertical exit slit opening;
- automatic alignment of the M3 focusing mirror using beam-wing current collectors located at the horizontal exit slits.

The endstation power supplies and controllers are integrated into the TANGO control system, enabling remote monitoring and control of heaters, power supplies, sample temperatures, and vacuum conditions. The sample manipulator is fully motorized, and the control software ensures precise and user-friendly positioning of the sample.

The beamline and endstation control environment is integrated with SES software (version 1.9, Windows 10), enabling the implementation of automated measurement sequences. This allows for fully programmable experiments once the sample has been positioned in front of the electron spectrometer. Typical automated workflows include multi-polarization and multi-spin component (curves or maps) measurements and k_z-dispersion mapping experiments. In addition, all beamline parameters and experimental settings used during a given measurement are automatically stored in the digital logbook.

Remote operation of the beamline via remote desktop access is also supported.

8.2. Igor Pro macros and URANOS Viewer for spectroscopy data analysis

To support the efficient data processing, viewing and the interpretation of both ARPES and spin-ARPES spectra, the URANOS beamline provides a dedicated package of Igor Pro macros and URANOS Viewer. These tools enable automated loading of experimental datasets and rapid visualization of three-dimensional photoemission data in multiple geometries, including isoenergetic and momentum-resolved slices.

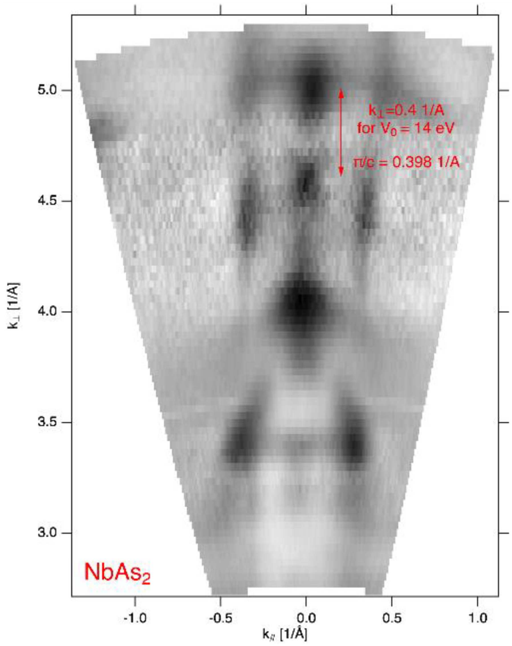

Fig. 13. Dispersion relation of $NbAs_2$ along the direction perpendicular to the surface (k_z), obtained by tuning the excitation energy in the range 20–100 eV. Further information about the sample can be found in [12].

Key functionalities include:

- data normalization and axis re-scaling,
- transformation of the measured distributions from angle-energy space to $\boldsymbol{k}$-energy space,
- flexible slicing and region-of-interest extraction,
- rotation and visualization of Fermi surface (FS) maps,
- band-structure mapping along arbitrary high-symmetry paths in the Brillouin zone,
- construction of FS maps as a function of excitation photon energy.

Macros and URANOS Viewer are implemented with a user-friendly graphical interface, ensuring intuitive operation even for users with limited prior experience with Igor Pro.

9. Performance and scientific output of the URANOS beamline

The URANOS beamline has achieved its design specifications, regarding photon flux and photon energy resolution. It has exceeded the specifications for the photon energy range useful for ARPES studies, so that it extends now from 8 to 150 eV. This range enables the acquisition of dispersive k_z maps (see Fig. 13), as well as resonant photoemission measurements [12].

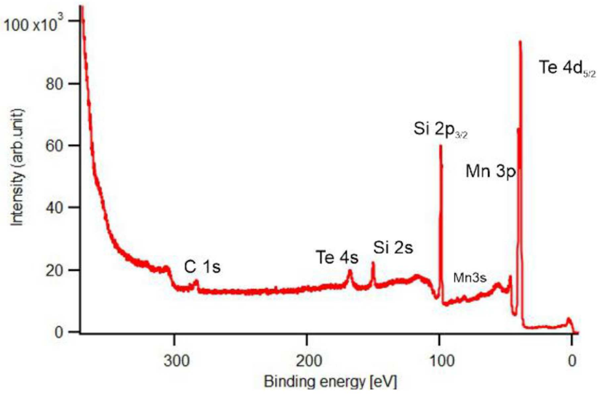

Fig. 14. XPS spectrum of $Mn_3Si_2Te_6$ recorded at an excitation energy of 400 eV.

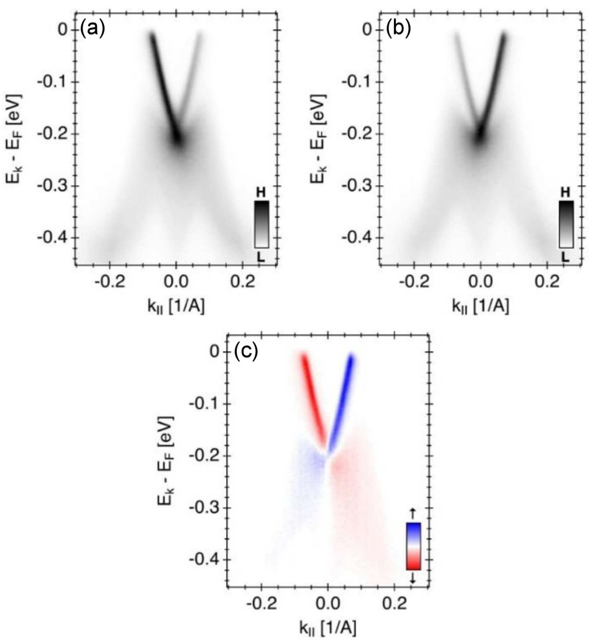

Fig. 15. ARPES spectra demonstrating circular dichroism in Bi_2Te_3 for left-circular polarization (a) and right-circular polarization (b), as well as their difference (c), at $h\nu = 55$ eV.

By operating the PGM monochromator close to the limits of its mechanical tuning range and by exploiting quasi-harmonics of the undulator, it is possible to generate monochromatic photon beams with energies up to 600 eV. Although the beamline transmission decreases significantly at such high photon energies, the flux remains sufficient for XPS-type, angle-integrated measurements, usefull for assessing the chemical composition of sample surface (see representative XPS data in Fig. 14).

Another important capability of the system is temperature-dependent ARPES, enabling the studies of phase transitions and temperature-induced modifications of the electronic band structure [13], as well as electron correlation effects [14, 15].

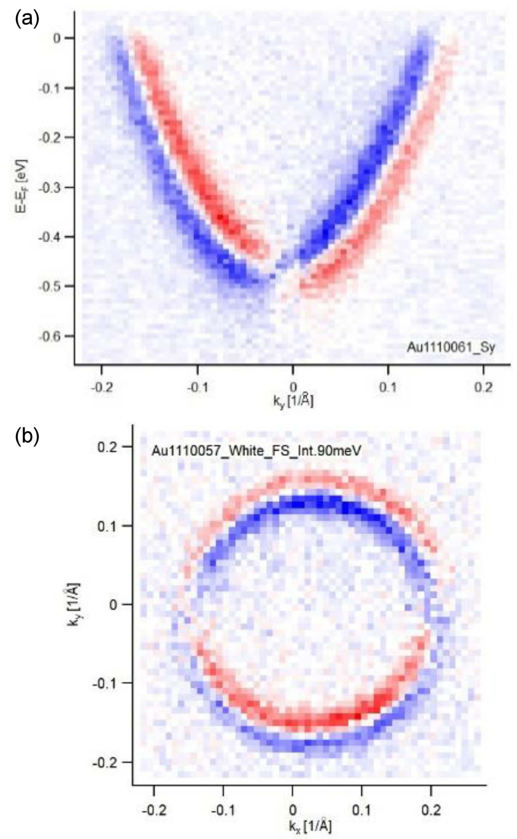

Fig. 16. Spin-resolved ARPES measurements (a) and the corresponding spin-resolved Fermi surface map (b) acquired for Au(111), showing the Rashba-split surface state associated with the herringbone reconstruction.

A further key functionality stems from the ability to tune the undulator phase, which enables circular dichroism measurements. Combined with spin-resolved detection, this allows for the separation of spin and orbital contributions in the measured photoemission spectra. Figure 15 shows the Bi_2Te_3 spectra measured with left- and right-circularly polarized light at a photon energy of $h\nu = 55$ eV, highlighting pronounced dichroic effects. Figure 16 presents spin-resolved measurements of the Au(111) surface, revealing spin landscape for the Rashba-split surface state.

Since its opening to users in 2018, the URANOS beamline has served approximately 150 experiments, resulting in 45 publications in high-impact journals to date. The research portfolio spans topological insulators [16–20], antiferromagnets [13, 21], frustrated lattices [22], superconductors [23, 24], Weyl semimetals [24–28], semiconductors [14, 15, 29], transition-metal dichalcogenides (TMDs) [30–32], and other two-dimensional materials [33–37]. For low-temperature measurements, users have routinely achieved a total energy resolution of 10 meV or better [10, 14, 15, 17–20, 29].

10. Conclusions

The URANOS beamline at the National Synchrotron Radiation Centre SOLARIS is a highly automated synchrotron-based platform dedicated to high-resolution ARPES and spin-resolved ARPES studies. The beamline combines a dual-monochromator optical system with undulator polarization control, enabling routine operation in the 8–150 eV photon energy range, with extension up to ≈ 600 eV for XPS-type and diagnostic measurements. The system achieves resolving powers of up to 20000 and low-meV energy resolution while maintaining stable beam delivery and high photon flux.

The experimental endstation integrates a VG Scienta DA30-L hemispherical spectrometer, a six-axis cryogenic manipulator, VLEED-based spin filters, and a comprehensive UHV sample preparation and characterization infrastructure. The beamline supports advanced momentum-resolved measurements, including k_z mapping, resonant photoemission, circular dichroism, and spin-resolved spectroscopy.

A high degree of automation and integration within the Tango-based and Python application control environment significantly streamlines experimental workflows and enables reproducible and efficient user operation. Combined with dedicated Igor Pro data-analysis tools and URANOS Viewer, this makes URANOS a versatile and accessible platform for modern electronic-structure investigations, ranging from routine band-structure characterization to advanced studies of spin-, orbital-, and temperature-dependent phenomena in quantum materials.

Acknowledgments

The beamline was constructed with funding from the Ministry of Education and Science and is operated at the National Synchrotron Radiation Centre SOLARIS, which is supported by the Polish Ministry of Science and Higher Education under contract No. 1/SOL/2021/2. We would like to thank the Hyades project team for providing the absorption data for the calibration gases.

References

[1] J. Szlachetko, J. Szade, E. Beyer et al., *Eur. Phys. J. Plus* **138**, 10 (2023).

[2] A.I. Wawrzyniak A. Marendziak, A. Kisiel et al., *Nucl. Instrum. Methods Phys. Res. B* **411**, 4 (2017).

[3] A. Kisiel, A. Marendziak, M. Ptaszkiewicz, A.I. Wawrzyniak, in: *Proc. 10th Int. Particle Accelerator Conf. (IPAC'19), Melbourne (Australia)*, JACoW Publishing, Geneva 2019, p. 3084.

[4] J. Wiechecki , A.I. Wawrzyniak, P. Król et al., in: *Proc. 7th Int. Particle Accelerator Conf. (IPAC2016), Busan (Korea)*, JACoW Publishing, Geneva 2016, p. 2902.

[5] A.I. Wawrzyniak, R. Panaś, A. Curcio, M. Knafel, G. Kowalski, A. Marendziak, *Nucl. Instrum. Methods Phys. Res. B* **493**, 19 (2021).

[6] J. Bahrdt, G. Wüstefeld, *Phys. Rev. ST Accel. Beams* **14**, 040703 (2011).

[7] M. Boots, D. Muir, A. Moewes, *J. Synchrotron Rad.* **20**, 272 (2013).

[8] H.-J. Hagemann, W. Gudat, C. Kunz, *J. Opt. Soc. Am.* **65**, 742 (1975).

[9] R. Follath, F. Senf, *Nucl. Instrum. Methods Phys. Res. A* **390**, 388 (1997).

[10] G. Grabecki, A. Dąbrowski, P. Iwanowski et al., *Phys Rev B* **101**, 085113 (2020).

[11] M.K. Fałowski, T.R. Noga, N. Olszowska, M. Zajac, in: *Proc. 17th Int. Conf. on Accelerator and Large Experimental Physics Control Systems (ICALEPCS2019), New York (NY)*, JACoW Publishing, Geneva 2020, p. 982.

[12] G. D'Olimpio, Y. Zhang, M. Rosmus et al., *Adv. Mater. Interfaces* **11**, 2300810 (2024).

[13] M. Hajlaoui, S. Wilfred D'Souza, L. Šmejkal et al., *Adv. Mater.* **36**, 2314076 (2024).

[14] J.J. Kolodziej, D. Wutke, M. Garb, N. Olszowska, M. Rosmus, *Appl. Surf. Sci.* **679**, 161195 (2024).

[15] D. Wutke, M. Garb, A. Krawczyk, A. Mielczarek, N. Olszowska, M. Rosmus, J. Kolodziej, *Phys. Rev. B* **107**, 155139 (2023).

[16] A.S. Wadge, K. Zberecki, B.J. Kowalski et al., *Phys. Rev. B* **110**, 35142 (2024).

[17] J. Polaczyński, G. Krizman, A. Kazakov et al., *Mater. Today* **75**, 135 (2024).

[18] D.A. Estyunin, T.P. Makarova, K.A. Kokh, O.E. Tereshchenko, A.M. Shikin, I.I. Klimovskikh, *Phys. Rev. B* **106**, 155305 (2022).

[19] I.I. Klimovskikh, D.A. Estyunin, T.P. Makarova, O.E. Tereshchenko, K.A. Kokh, A.M. Shikin, *J. Phys. Chem. Lett.* **13**, 6628 (2022).

[20] J. Sitnicka, K. Park, P. Skupiński et al., *2d Mater.* **9**, 015026 (2022).

[21] M. Zeng, P. Liu, M.-Y. Zhu et al., arXiv:2511.02447, 2025.

[22] P. Rezende-Gonçalves, A. Antezak, T. Kato et al., *Phys. Rev. B* **111**, 205114 (2025).

[23] R. Kurleto, M. Fidrysiak, L. Nicolaï et al., *Phys. Rev. B* **104**, 125104 (2021).

[24] A.S. Wadge, G. Grabecki, C. Autieri et al., *J. Phys. Condens. Matter* **34**, 125601 (2022).

[25] A.S. Wadge, B.J. Kowalski, C. Autieri, P. Iwanowski, A. Hruban, N. Olszowska, M. Rosmus, J. Kolodziej, A. Wisniewski, *Phys. Rev. B* **105**, 235304 (2022).

[26] G. D'Olimpio, Y. Zhang, M. Rosmus et al., *Adv. Mater. Interfaces* **11**, 2300810 (2024).

[27] F. Mazzola, Y. Zhang, N. Olszowska et al., *J. Phys. Chem. Lett.* **14**, 3120 (2023).

[28] J. Bermejo-Ortiz, G. Krizman, R. Jakiela, Z. Khosravizadeh, M. Hajlaoui, G. Bauer, G. Springholz, L.-A. de Vaulchier, Y. Guldner, *Phys. Rev. B* **107**, 075129 (2023).

[29] G. Krizman, T. Zakusylo, L. Sajeev et al., *Adv. Mater.* **36**, 2310278 (2023).

[30] J. Obando-Guevara, Á. González-García, M. Rosmus, N. Olszowska, C. González, M.Á. González-Barrio, A. Tejeda, A. Mascaraque, *ACS Nano* **19**, 2540 (2025).

[31] J. Obando-Guevara, Á. González-García, M. Rosmus, N. Olszowska, C. González, G. Morón-Navarrete, J. Fujii, A. Tejeda, M.Á. González-Barrio, A. Mascaraque, *J. Mater. Chem. A* **12**, 24694 (2024).

[32] Y.U. Boucher, I. Biało, M.A. Gala et al., *Phys. Rev. B* **109**, 85135 (2023).

[33] M. Cameau, T. Cren, P. David, F. Debontridder, N. Olszowska, M. Rosmus, M. Silly, M. D'angelo, *Phys. Rev. B* **110**, 205414 (2024).

[34] M. Cameau, N. Olszowska, M. Rosmus, M.G. Silly, T. Cren, A. Malecot, P. David, M. D'angelo, *2D Mater.* **11**, 35023 (2024).

[35] A. Tołłoczko, J. Ziembicki, M. Grodzicki, J. Serafińczuk, M. Rosmus, N. Olszowska, S. Gorantla, M. Erdi, S. Tongay, R. Kudrawiec, *Small* **21**, 2410903 (2025).

[36] A.K. Tołłoczko, S.J. Zelewski, J. Ziembicki, N. Olszowska, M. Rosmus, T. Woźniak, S. Tongay, R. Kudrawiec, *Adv. Opt. Mater.* **12**, 2302049 (2023).

[37] S. Kamal, I. Seo, P. Bampoulis et al., *ACS Appl. Mater. Interfaces* **15**, 49 (2023).